Chemical Engineering Science 325 (2026) 123467

Contents lists available at ScienceDirect

Chemical Engineering Science

journal homepage: www.elsevier.com/locate/ces

Reactivity influence on carbonaceous particle layer break-up and relocation events in O_2-based model filter regeneration

Ole Desens [a,*], Özge Yavuz [a], Fabian P. Hagen [b], Jörg Meyer [a], Achim Dittler [a]

[a] Karlsruhe Institute of Technology (KIT), Institute of Mechanical Process Engineering and Mechanics (MVM) - Gas Particle Systems, Straße am Forum 8, Karlsruhe, 76131, Germany
[b] Karlsruhe Institute of Technology (KIT), Engler-Bunte-Institute (EBI) - Combustion Technology, Engler-Bunte-Ring 7, Karlsruhe, 76131, Germany

ARTICLE INFO

Keywords:
High-speed imaging
Particulate filters
Soot
Oxidation
Regeneration

ABSTRACT

Understanding the influence of soot reactivity on layer break-up and particle structure detachment and transport during diesel particulate filter regeneration is essential for optimizing aftertreatment performance. Seven carbon blacks with differing reactivity were investigated as reactive particle model systems. The oxidation behavior was characterized by temperature-programmed oxidation, revealing a wide reactivity range, with the peak oxidation temperature spanning from 817 K for a propane-soot reference to 894-976 K for the carbon blacks. This paper examines the regeneration of a model filter channel in situ with high temporal and spatial resolution. The filter is loaded with 10 mg carbon black particles and then regenerated. The regeneration of the filter is analyzed by varying the particle system under constant regeneration conditions at a gas temperature of 823 K and a channel inlet gas velocity of 60 m/s. In addition, the layer height and temperature are varied for a selected carbon black, and a more reactive hydrocarbon mixture was added to the particle layer of the selected carbon black. In selected experiments high-speed imaging of the model filter channel enabled direct observation of layer break-up and particles detaching from the filters surface. Image-based analysis enables the quantification of the black surface area reduction and isolated particle structures. All carbon blacks showed a reaction of the carbonaceous particles, with little layer break-up and formation of isolated structures, as well as minimal detachment events (0-10 events per experiment). Introducing more reactive hydrocarbons to the particle layer markedly increased fragmentation and particle relocations to more than 500 events.

1. Introduction

Environmental protection and air quality are essential for safeguarding human health. The revised EU Air Quality Directive 2024/2881 European Commission (2025) sets a monitoring requirement of black carbon and ultrafine particles, which have adverse impacts on human health and climate. Removal of combustion-generated soot remains a critical challenge for both engine performance and air quality. According to the European Commission in Annex I, Table 2 of Regulation No 715/2007 European Commission (2020), the Euro 6 emission limit is 6.0×10^{11} particles per km for particles. In addition, from November 2026, the Euro 7 lower particle size threshold will be tightened to ≥ 10 nm (instead of the previous ≥ 23 nm) Parliament (2024). Diesel particulate filters (DPF) and gasoline particulate filters (GPF/OPF) are essential for trapping soot and ash. The particle-laden exhaust gas aerosol flows into the inlet channels of the filter, where it passes through the filter walls, depositing particles on and within the porous filter walls. This process leads to an accumulation of particles and thus, the formation of a particle layer, which increases the pressure drop Ishizawa et al. (2009), Sappok et al. (2014). Consequently, the filter is regenerated regularly by an increased exhaust gas temperature. As a result, soot particles oxidize, causing the layer to break up and allowing individual particle structures to be transported Thieringer et al. (2023), Sappok et al. (2013). The filtration efficiency and pressure drop are directly influenced by the structure of the deposited soot layer and by whether the deposit develops in a homogeneous residual layer or plug-end pattern after repeated regenerations Dittler (2017), Gaiser and Mucha (2004), Frank and Hardenberg (1985), Konstandopoulos and Johnson (1989), Choi et al. (2014), Tandon et al. (2010), Cui et al. (2018). Bensaid et al. Bensaid et al. (2010) found that, while low regeneration temperatures can produce a nearly uniform consumption of the soot cake, higher temperatures (≥ 873 K) cause ignition to start at the inlet and propagate downstream towards the end of the filter channel, which becomes the hottest region of the filter. The effectiveness of regeneration is governed not only by process parameters (temperature, flow velocity, layer thickness), but also by the soot's oxidative behavior. High-resolution

* Corresponding author.
E-mail address: ole.desens@kit.edu (O. Desens).

https://doi.org/10.1016/j.ces.2026.123467
Received 15 December 2025; Received in revised form 19 January 2026; Accepted 27 January 2026
Available online 29 January 2026

microscopy and spectroscopy over the past decade have revealed that primary soot particles comprise graphene-layer stacks, polyaromatic fragments, and edge-bonded functional groups whose arrangement varies with fuel type, engine conditions, and post-formation treatment, all of which affect oxidation kinetics Wal and Tomasek (2003), Boehman et al. (2005), Song et al. (2006), Lindner et al. (2015), Koch et al. (2022). A wide range of studies have demonstrated that soot reactivity varies significantly depending on its source and formation conditions. Some studies have shown that Biodiesel-derived soot can be more reactive than fossil diesel soot, with reactivity increasing with higher biofuel content and operating pressure Song et al. (2006), Ess et al. (2016), Lapuerta et al. (2012), Soriano et al. (2017). Alternative fuels such as Gas-to-Liquid fuel (GTL), Hydrotreated Vegetable Oil (HVO), Hydrotreated Renewable Diesel (HRD), or Oxymethylene Ethers (OMEx) also produce soot with distinct reactivities Böhmeke et al. (2024), Alhikami et al. (2022). Zhou et al. Zhou et al. (2025) simulated n-butanol/n-octanol and n-butanol/di-n-butyl ether dual-fuel engines across premixed fuel fractions. They found approx. 40 % reduction in soot particle number for the butanol/n-octanol engine at B10 and a decrease of four to five orders of magnitude as the premixed fraction rises from B10 to B90. Several works underline that reactivity is not simply correlated with particle size or surface area, but is strongly governed by nanostructure: soot with smaller, disordered graphene fringes tends to be more reactive, whereas larger, ordered structures reduce reactivity Hagen et al. (2021a,b), Liati et al. (2013), Chen et al. (2024). Additives, such as 2,5-Dimethylfuran (DMF) or methanol blends, further enhance amorphous character and thereby increase oxidation rates Chen et al. (2024), Gogoi et al. (2015). Collectively, these findings highlight that soot from different sources exhibits highly diverse reactivity, which is determined not only by the fuel type but also by formation pathways and engine operation.

Two soot oxidation pathways with oxygen (O_2) are commonly distinguished: surface oxidation and internal oxidation. Surface oxidation involves reaction of O_2 at outer surfaces; internal oxidation occurs when oxygen diffuses into soot pores and reacts within particle interiors. At moderate temperatures (< 1100 K), internal diffusion is feasible, and oxide reactions occur throughout the soot bulk, often resulting in hollows or increased surface area. At higher temperatures, oxidation becomes surface-limited as reaction rates outpace diffusion. Hagen et al. (2021a), Kelesidis and Pratsinis (2019), Ghiassi et al. (2016)

Fu et al. Fu et al. (2026) used high-resolution transmission electron microscopy (HRTEM) and Raman spectroscopy to monitor soot structure during realistic DPF regeneration at inlet temperatures of 573 K and 623 K. At 573 K, micropore growth led to internal burning and hollow interiors, indicating internal burning, whereas at 623 K soot underwent uniform surface oxidation and the soot structure remained more ordered.

During particulate filter regeneration, dynamic processes of layer break-up, formation of 'soot islands', particle detachment and transport have been visualized. Sappok et al. Sappok et al. (2013) visualized a small diesel particulate filter section during regeneration using a microscope to observe initial soot layer break-up and downstream transport. Thieringer et al. Thieringer et al. (2023) visualized the entire channel length demonstrating that higher gas velocities lead to more relocating events of particle structures, while higher temperatures accelerate oxidation rates and also lead to more relocating structures. Numerical Lattice-Boltzmann simulations further indicate that shear forces near the inlet favor detachment, whereas downstream regions exhibit reduced relocations Hafen et al. (2023). Governing these dynamics, interparticle cohesive forces are often much higher than adhesion between soot and the soot filter surface structure Kamp et al. (2014). To meet stricter emission regulations and adapt to alternative renewable fuels, deeper understanding of regeneration phenomena is needed. Carbon black (CB) with a controlled, reproducible structure and thus specifically comparable reactivity serves as a model particle system because it reduces the variability inherent in real engine soot. Carbon blacks differ from engine-generated soot primarily in composition and post-treatment. Both materials consist of fractal-like agglomerates of nanoscale primary particles. Zhang et al. Zhang et al. (2022) showed that a commercial carbon black can closely match gasoline direct injection (GDI) exhaust soot across key physicochemical properties, including fractal dimension, gyration radius, primary particle size, fringe length, separation distance, tortuosity, carbon content and apparent activation energy. Industrial carbon blacks are produced in quenched heavy-oil flames, i.e., in a partial-oxidation process of long-chain hydrocarbons (HC) Zainol et al. (2025). This yields agglomerates of nearly pure elemental carbon with reproducible primary particle sizes, surface areas, and degrees of nanostructural order, but without the inorganic ash, condensed volatile organic fraction (VOF) or condensed soluble organic fractions (SOF) typically present in engine soot M and Maricq (2007), Clague et al. (1999). SOFs consists of semi-volatile hydrocarbons, with polycyclic aromatic hydrocarbons (PAHs) forming an important subgroup of these species. The amount and composition of SOF have been shown to modify soot oxidation behavior in TPO experiments shifting apparent reactivity Liu et al. (2017), Huang et al. (2024). These organics can form sub-nanometer liquid films and capillary bridges between primary soot particles, which strongly promote aggregate restructuring and compaction Chen et al. (2016), Corbin et al. (2023), Schnitzler et al. (2017). Shao et al. Shao et al. (2023) showed that nascent soot is rich in peri-condensed PAHs whose van der Waals interactions are strong enough to form stable dimers and clusters, i.e. soot inception can proceed by purely physical binding. Rothenbacher et al. Rothenbacher et al. (2008) demonstrated that aged diesel soot agglomerates exhibit bond energies about two orders of magnitude higher than theoretical estimates for van-der-Waals-bound nanoparticle clusters. Reproducing this complexity in a single engine test campaign is challenging. Using carbon blacks with consistent reactivity as a model system allows to systematically test how the reactivity of carbonaceous particles affect regeneration phenomena. While carbon blacks and the model filter channel are surrogate systems that mimic key aspects of the real-world application, they enable mechanistic investigations under well-defined boundary conditions, which cannot be achieved under realistic operating conditions. In this study, the relationship between particle layer break-up and rearrangement processes during filter channel regeneration is investigated by comparing seven different CB layers in a model filter channel. Layer break-up, particle detachment, and transport along a complete model filter channel are analyzed using high-speed imaging.

2. Materials and method

2.1. Model systems

To investigate the influence of soot reactivity and dispersity on regeneration phenomena within the model filter channel, seven carbon blacks were selected as reactive particle systems. They were partially compared with a highly reactive soot system generated in fuel-rich propane combustion (PS-T817) using the MiniCAST 6204C soot generator (Jing Ltd., Zollikofen, Switzerland). Data for PS-T817 were taken from previous studies using the soot generator and the model filter channel Thieringer et al. (2023), Desens et al. (2025a). The selected CBs span a wide range of nanostructural and oxidative properties, thereby covering a spectrum of reactivities and dispersities. All CBs are obtained from industrial furnace black production, except CB-T900, which is a lamp black. Fig. 1 presents the scanning electron microscopy (SEM) images of the particle systems. Based on SEM images, estimated primary particle sizes range from a count median diameter (CMD) of approximately 26 nm to 123 nm. PS-T817 exhibits the highest oxidation reactivity, while CB-T976 represents the least reactive sample. The carbon blacks were named according to their temperature of maximum oxidation rate T_{max} from temperature-programmed oxidation (TPO), which allows their reactivity to be classified by designation. T_{max} is a key indicator of soot reactivity, a higher T_{max} means lower reactivity Hagen et al. (2021a). The reactivity of the particle systems was

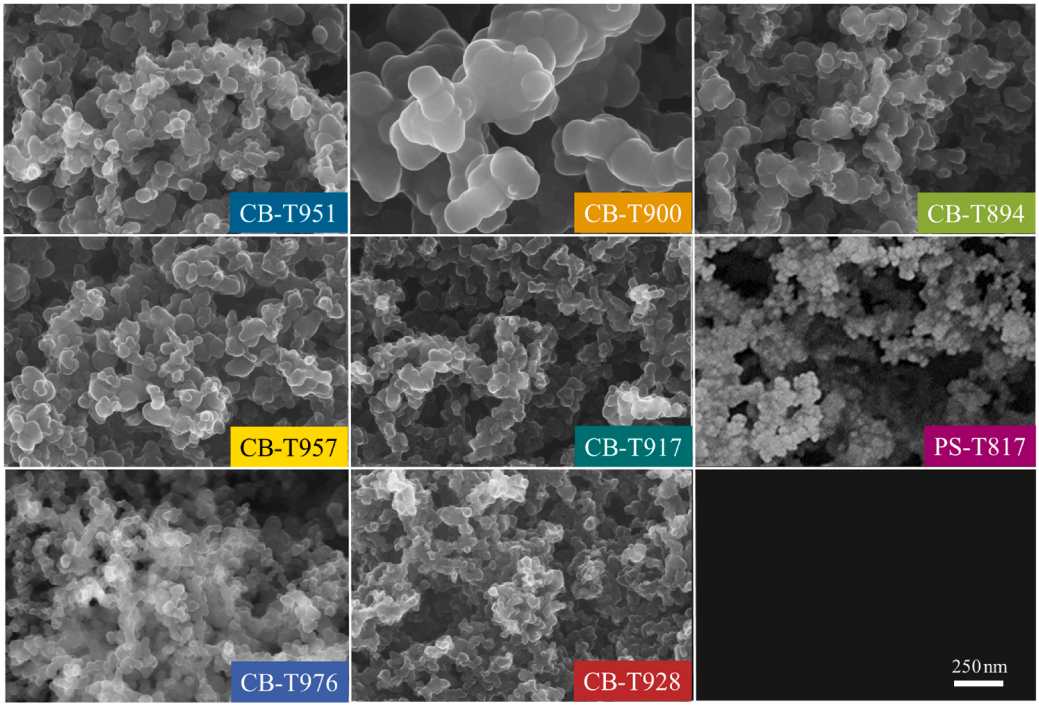

Fig. 1. SEM images of the investigated particulate systems, recorded at an accelerating voltage of 10.0 kV, a magnification of 100 kX, and a working distance of 5.7 mm.

determined by TPO under dynamic, non-isothermal conditions using a TG 209 F1 Libra thermobalance (Netzsch Gerätebau GmbH, Germany). Each sample was prepared with an initial mass of $m_0 = 2 \pm 0.2$ mg and heated from ambient temperature to 1200 K at a constant heating rate of $\beta = 5$ K/min in an oxidizing atmosphere composed of 21 vol.% O_2 and 79 vol.% N_2. TPO was performed under a constant heating rate to obtain $d\alpha/dT$ profiles and a well-defined T_{max} for inter-sample reactivity ranking and global kinetic fitting. A moderate heating rate (5 K/min) was selected to minimize thermal lag while maintaining adequate temperature resolution. The final temperature (1200 K) ensures complete oxidation even for low-reactivity samples. This procedure is consistent with established soot TPO protocols Messerer et al. (2006), Schmid et al. (2011), Knauer et al. (2009), Sharma et al. (2012).

The oxidation rate was derived from the differential mass-loss rate, $d\alpha/dT$, where α denotes the fractional mass conversion. As temperature increases, the oxidation rate rises up to T_{max} due to the thermally activated acceleration of reaction kinetics. Beyond T_{max}, the rate declines as the reactive carbon is progressively consumed. Lower T_{max} values therefore correspond to higher soot reactivity, whereas higher T_{max} values indicate more inert behavior. To describe the temperature dependence of oxidation, a global kinetic approach proposed by Hagen et al. Hagen et al. (2021a) was applied based on the Arrhenius equation:

$$\frac{d\alpha}{dT} = -k_{ox} \cdot \alpha^n = -k_{0,ox} \cdot exp\left(\frac{-E_a}{R \cdot T}\right) \cdot \alpha^n, \tag{1}$$

where k_ox is the oxidation rate coefficient, $k_{0,ox}$, the pre-exponential factor, Ea the apparent activation energy, n the overall reaction order, R the universal gas constant, and T the absolute temperature. The kinetic parameters were obtained by fitting the model to the experimental TPO curves using the Levenberg-Marquardt optimization method Marquardt (1963), Levenberg (1944). To enable a quantitative comparison of reactivity across the carbon blacks and the PS-T817 reference, a dimensionless reactivity index $RI_{823K,i}$ was defined at the regeneration temperature of 823 K under 21 vol.% O_2. The index normalizes the logarithmic oxidation rate of each sample relative to the least reactive CB-T976 ($RI_{823K,CB-T976} = 0$) and most reactive PS-T817 ($RI_{823K,PS-T817} = 1$):

$$RI_{823K,i} = \left[\frac{ln\{ox.\ rate\}_{CB-T976} - ln\{ox.\ rate\}_{i,\ T_{reg}}}{ln\{ox.\ rate\}_{CB-T976} - ln\{ox.\ rate\}_{PS-T817}}\right]_{823\ K,21\ vol.\%} \tag{2}$$

Fig. 2 a) shows the TPO profiles of the investigated carbon blacks (CB-T894, CB-T917, CB-T928 and CB-T976) in comparison with the highly reactive PS-T817 reference. PS-T817 exhibits the lowest temperature at the maximum oxidation rate ($T_{max} = 817$ K), confirming its higher reactivity compared with the carbon blacks. Among the CB grades, T_{max} systematically increases from CB-T894 (894 K) to CB-T976 (976 K), indicating progressively lower oxidation reactivity. These values lie within the temperature range typically reported for diesel soot (786 - 935 K) under engine-relevant conditions Lindner et al. (2015), Hagen et al. (2021a). Additionally, PS-T817 shows a minor peak around 400 K, attributed to the desorption and oxidation of volatile organic compounds formed during soot generation in the MiniCAST 6204C. This low-temperature signal is absent in the carbon blacks, which contain virtually no volatile organic fractions. The normalized reactivity index RI_{823K} (as shown in Fig. 2 b) and summarized in Table 1), decreases from 1 for PS-T817 to 0 for CB-T976, with intermediate values for the carbon blacks reflecting their graded oxidative behavior. CB-T894 and CB-T900 exhibit relatively high reactivities ($RI_{823K,CB-T894} = 0.83$), while CB-T917, CB-T951, and CB-T957 show lower values between 0.5 and 0.7. Plotting RI_{823K} against the CMD confirms that reactivity does not depend directly on primary particle size, but rather, as shown by Hagen et al., on the arrangement and length of the fringes Hagen et al. (2021a). The kinetic parameters obtained from model fitting (see Table 1) demonstrate that the investigated carbon blacks exhibit a broad range of oxidation behaviors, spanning nearly 160 K in T_{max} and covering more than one order of magnitude in apparent rate constants, from 8.05×10^5 s^{-1} to 1.28×10^7 s^{-1}. The reaction order n ranges between 0.07 and 0.64 for the carbon blacks, indicating varying oxidation mechanisms and active-site distributions compared with PS-T817 ($n = 1.39$). Distinct oxidation characteristics are observed for CB-T928, CB-T951, and CB-T957. These samples display an abrupt mass-loss event once a critical temperature is reached, leading to complete oxidation within only a few minutes.

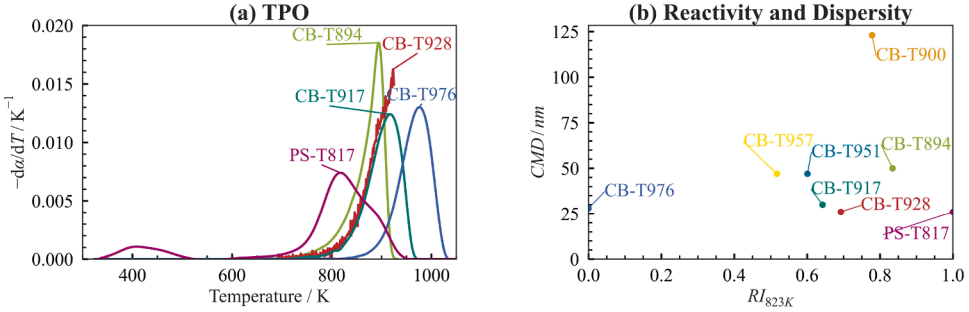

Fig. 2. a) Temperature-programmed oxidation (TPO) profiles of the investigated carbon blacks (CB-T894, CB-T917, CB-T928 and CB-T976) in comparison to the PS-T817 reference , $c_{O_2} = 21 vol.\%$, $c_{N_2} = 79\, vol.\%$, heating rate $\beta = 5$ K/min b) Reactivity distribution of the carbon blacks (CB-T894 to CB-T976), expressed as the normalized reactivity index at 823 K (RI_{823K}), and the count-mean diameter (CMD) obtained from the SEM images.

Table 1
Properties of the investigated particulate systems ordered by decreasing reactivity.

Particle system	CMD /nm	BET /m^2g^{-1}	C-H ratio	T_{max} /K	$k_{0,ox}$ /s^{-1}	n	E_a /kJ mol^{-1}	R^2	$RI_{823\,K}$
PS-T817[a)]	26	70–120[b)]	-	817	8.05×10^5	1.39	137	0.95	1.00
CB-T894	50	-	10	894	4.81×10^6	0.43	160	0.96	0.83
CB-T900	123	-	11	900	5.52×10^6	0.45	162	0.97	0.78
CB-T928	26	90	18[c)]	928	9.38×10^6	0.35	170	0.99	0.69
CB-T917	30	254	15	917	6.23×10^6	0.64	167	0.99	0.64
CB-T951	47	48	-	951	1.25×10^7	0.35	177	0.94	0.60
CB-T957	47	48	19[c)]	957	9.92×10^6	0.07	178	0.92	0.52
CB-T976	28	62	19	976	1.28×10^7	0.64	184	0.98	0.00

[a)] Data from Desens et al. (2025a). [b)] Data from Mahrt et al. (2018). [c)] Data from Hagen et al. (2021b).

Such rapid transitions suggest a chain-reaction-like mechanism, possibly triggered by local restructuring of the carbon surface or the sudden exposure of active sites after partial gasification. In contrast, PS-T817 and the other CBs oxidize more gradually.

2.2. Experimental setup and procedures

The experimental setup and the model filter channel used can be seen in Fig. 3. The model filter channel Thieringer et al. (2023) consists of a rectangular channel with a sintered metal filter element (filtration area: 3 mm × 120 mm). A 5 mm inlet section extends the area before the flow passes through the sintered metal filter to promote a quasi-steady flow with minimal vortex formation. The channel height is 4 mm. The inlet channel is equipped with a quartz glass window at the top to enable optical access during regeneration. The stainless-steel housing (1.4841) is sealed with high-temperature gaskets.

The experimental procedure comprises three phases: (1) particle layer formation at ambient temperature and 13.2 m/s inlet velocity, (2) system heating under inert gas (N_2), and (3) oxidation and regeneration under particle free air flow. During layer formation, carbon black particles were dispersed using a dust generator (SAG 410/U, TOPAS GmbH) and deposited in the model filter channel at an inlet gas velocity of 13.2 m/s and ambient temperature (293 K) under air atmosphere until the desired soot mass was reached. The inlet velocity was chosen based on preliminary loading experiments demonstrating homogeneous layer deposition without a tendency toward plug-end-filling patterns, while enabling rapid and reproducible filter loading Thieringer et al. (2023). Air and nitrogen are supplied via thermal mass-flow controllers. For regeneration, the system was preheated under nitrogen and then switched to air as the oxidation gas when the desired temperature is reached. The inlet gas velocity was increased to 60 m/s, and the oxidation gas temperature was maintained at 823 K. Temperature control during regeneration is achieved through synchronized regulation of the oven and heating plate, with PT100 sensors at the inlet and outlet of the model filter channel. The regeneration experiments were recorded using a high-speed camera (CP90-25P-M72, Optronis GmbH) positioned perpendicularly to the model filter channel through a quartz glass window. Illumination was provided by two LED panels (GSVitec MultiLed G8, QT + G8) with a luminous flux of $\Phi = 12,000$ lm and a power of $P = 150$ W each. The camera is equipped with a Zeiss Milvus 2/100M macro lens. During regeneration, the frame rate was initially set to 100 fps and increased to 1000 fps once visible layer break-up occurred.

2.3. Image analysis

Custom Python scripts were employed for subsequent image analysis, focusing on the quantification of soot layer reduction and break-up as well as particle structures detaching from the filter surface in the high-speed video data. Layer break-up and layer reduction analysis were performed using the image-processing workflow previously described by Desens et. al. Desens et al. (2025a). The method combines pre-processing, threshold-based segmentation, and geometric evaluation of regions of interest (ROIs). Contrast and noise were optimized by grayscale conversion, exposure adjustment, and Gaussian smoothing. Otsu's method and morphological filtering (erosion, dilation, opening) were applied to isolate soot structures, from which geometric properties were extracted and converted to physical units. The onset of layer break-up was defined as the time when 90 % of the black surface layer remained in the visible layer area. Measurement uncertainty was quantified using a Monte Carlo-based variation of segmentation parameters by ± 5 %. For the detection and verification of particle structure detachments during filter regeneration, a semi-automated Python-based image analysis workflow Desens et al. (2025b) is used. The method follows a two-step procedure specifically designed to identify and validate small particle structures (100-1000 µm) detaching from the filter surface in high-speed video sequences containing up to several million frames. In Step 1 (Detection), OpenCV's MOG2 background-subtraction algorithm was applied with a learning rate of 0.1 and a history length of 1000 frames. Candidate detachment events were then extracted based on contour features, using user-defined thresholds for size and aspect ratio.

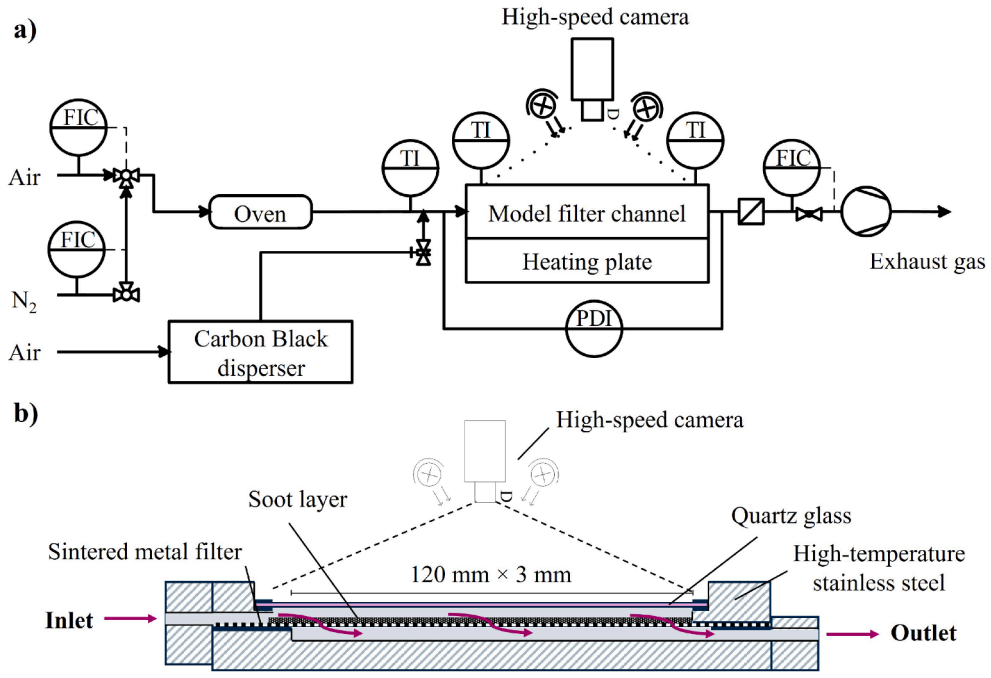

Fig. 3. a) The experimental setup used b) the model filter channel Thieringer et al. (2023).

In Step 2 (Verification), the algorithm analyzes the areas surrounding potential detachments by applying binary thresholding and generating absolute difference images between consecutive frames. Morphological opening operations were employed to suppress noise, and a detachment event was confirmed when the difference area exceeded 20 px, corresponding to an equivalent diameter of approximately 100 µm. The workflow outputs include particle identification numbers, spatial coordinates, equivalent diameters, frame indices, and binary probability values (0 or 1) indicating detection confidence. The frames at which the detachment was detected are saved with the respective difference images so that they can be double-checked manually afterward.

3. Results and discussion

3.1. Regeneration behavior with variation of the particle system

Initially, all carbon blacks were examined under identical regeneration conditions in the model filter channel. The regeneration experiments were performed using particle-free compressed air as the oxidizing medium at a constant gas temperature of 823 K and a inlet gas velocity of 60 m/s. All filters were loaded with a soot mass of 10 ± 1 mg. The soot layer height was quantified using laser scanning microscopy (LSM, VK-X100K/X200K, Keyence GmbH, Germany). For each sample, three representative regions along the channel axis (inlet, center, outlet) were imaged at 10× magnification. The average layer height was obtained from the difference between the mean height of the loaded and unloaded filter areas. The measured soot-layer heights ranged from approximately 150 µm to 250 µm, depending on the type of carbon black. Thinner layers were obtained for CB-T957 (~150 µm), CB-T951 (~175 µm), and CB-T928 (~170 µm), while CB-T917 (~250 µm) and CB-T900 (~210 µm) formed the thicker deposits. The final differential pressure during filter loading at 13.2 m/s reflected particle-size-dependent packing: CB-T894 ($CMD \approx 50$ nm) reached 19 mbar, CB-T900 ($CMD \approx 123$ nm) showed the lowest value (10 mbar), and the fine and dense CB-T928 ($CMD \approx 26$ nm) produced 36 mbar.

After the deposition of the layer and the subsequent heating of the oven, pipes, and model filter channel, the system switches from N_2 to particle-free air, thereby initiating the regeneration phase ($t = 0$ min).

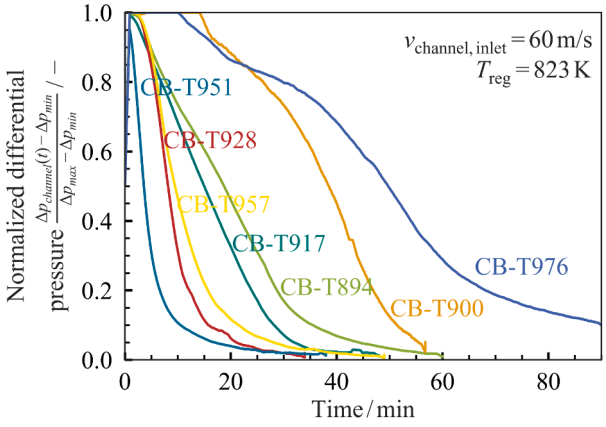

Fig. 4. Normalized differential pressure during regeneration of the model filter channel at 823 K loaded with the carbon black particle systems.

Fig. 4 shows the normalized differential pressure as a function of time during regeneration of the model filter channel at 823 K. All samples exhibit a decrease in pressure drop as soot oxidation progresses. The maximum differential pressure at the start of regeneration was normalized to 1, with 0 representing the pressure drop of a fully regenerated, soot-free filter. With the exception of CB-T976 and CB-T900, all carbon blacks exhibited a rapid decrease in pressure within the initial 30 to 40 min, suggesting effective carbonaceous particle removal. Conversely, the least reactive sample, CB-T976, exhibited a markedly slower rate of regeneration and an incomplete regeneration after 90 min. The observed regeneration rates generally align with the reactivity trends derived from the TPO analysis, indicating that materials with higher reactivity indices (RI_{823K}) exhibit faster oxidation and shorter regeneration times. It is noteworthy that CB-T928, CB-T951, and CB-T957 systems exhibit a very rapid decline in pressure drop and accordingly brief regeneration time of less than 40 min. This observation is consistent with the pronounced mass-loss events observed in TPO, wherein these materials underwent complete oxidation within a

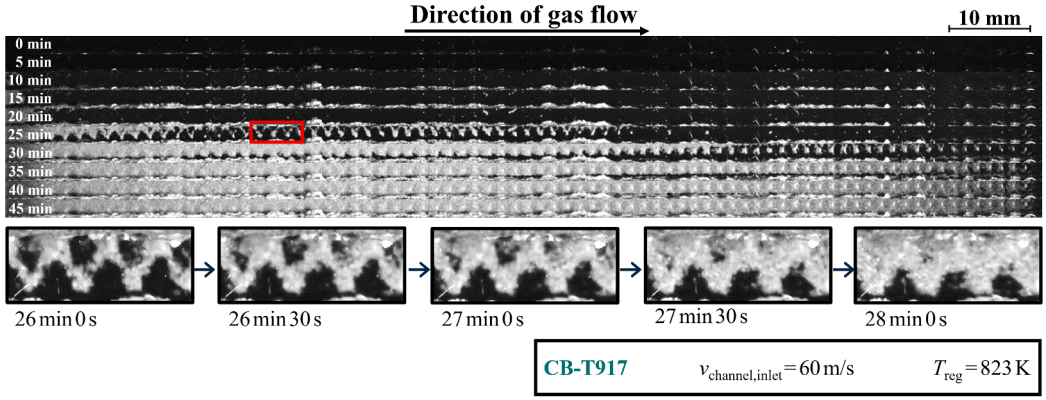

Fig. 5. Time-resolved image sequence of the regeneration process of CB-T917, illustrating the progression from the initiation of regeneration 0 min to 45 min over the entire channel length. The region marked by the rectangle is shown magnified below, illustrating the oxidation of structural sizes between 26 min and 28 min.

span of few minutes when oxidized in air. The lower soot-layer heights measured for these samples may have further enhanced oxygen accessibility to the active zones. In contrast, CB-T900, despite its relatively low T_{max}, exhibits a longer regeneration time, which may be attributable to its significantly larger particle size ($CMD \approx 123$ nm). The deviations between kinetic parameters and the observed regeneration behavior likely result from altered mass and heat transfer within the dense soot layer, where variations in layer height and morphology may alter gas permeability and local heat transfer.

3.1.1. Visual layer break-up

The high-speed recordings are evaluated to show the differences of the carbonaceous particle layers during filter regeneration in the experiments. As illustrated in Fig. 5, a representative sequence of the regeneration process for CB-T917 was recorded over a period of 45 min at a temperature of 823 K.

At 0 min, a continuous dark carbon black layer covers the entire channel surface. After approximately 15 min, the first openings appear near the channel inlet, indicating the onset of localized oxidation. By 25 min, the soot layer has fractured across approximately two-thirds of the channel's length, forming a zigzag break-up pattern. The oxidation front continues to propagate downstream until the layer is completely removed after approximately 45 min. The magnified sequence in Fig. 5 illustrates the local temporal evolution of the particle structures between 26 min and 28 min. During this short interval, the structures shrink progressively from the outer edge towards the center until they oxidize completely. Only few isolated particle structures persist, the structures oxidize rapidly once exposed to the O_2-rich gas phase.

Fig. 6 compares the time-resolved regeneration sequences for all investigated carbon blacks under identical boundary conditions (823 K, 60 m/s, particle-free air). The soot layer continuously oxidizes from the inlet toward the outlet, with residual structures persisting longest in the rear section of the channel. In contrast to the findings of Sappok et al. Sappok et al. (2013) and Thieringer et al. Thieringer et al. (2023), the carbon blacks exhibit very little formation of isolated particle structures ('islands of soot'). This observation aligns with the results of Desens et al., where a similar carbon black showed comparable behavior Desens et al. (2025a). To quantify the visual observations, image analysis was conducted for each frame at 5 min intervals. The black surface area fraction, which represents the remaining soot coverage, and the number of isolated particle structures were extracted as functions of regeneration time. Fig. 7 summarizes these results for the carbon blacks (CB-T894 to CB-T976).

In Fig. 7 a), the black surface area fraction decreases continuously during regeneration. However, it initially remains stable above 0.9. Once the CB layer has broken up further after the onset of layer break-up, the area covered with particles decreases rapidly. The onset of layer break-up, indicated in the curves as the time at 10 % loss in CB-covered surface, occurs e.g. for CB-T917 at 16 min, followed by CB-T894 (32 min) and CB-T976 (47 min). Fig. 7 b) shows the temporal evolution of the number of structural sizes, which quantifies the amount of isolated particle structures identified in each frame. For CB-T894 and CB-T917, the number of structures increases once the layer break-up begins, followed by a decline as these structures oxidize. In contrast, CB-T976 exhibits a delayed and broader distribution with less isolated structures, consistent with slower oxidation. The maximum number of isolated structures observed during regeneration ranged between 50 and 150 for all CBs. The variability of this metric is considerable, as the threshold for segmentation and subsequent morphological operations exerts a substantial influence on the detected structure count. The error range is indicated in the diagram, as described in Section 2.3. For comparison, Desens et al. reported more than 300 isolated structures during the regeneration of PS-T817, highlighting the substantially higher fragmentation tendency as visualized in Fig. 8 Desens et al. (2025a).

3.1.2. Relocations of particle structures

Using the methodology described in Section 2.3, the high-speed recordings were scanned for particle structure detachment events and particle transport. The analysis of each experiment involved the examination of several million frames. As shown in Fig. 9, a representative detachment event of a particle structure relocating was observed for CB-T917 after 27 min, corresponding to an advanced stage of regeneration in which part of the filter surface was already free of soot. The upper frames show the complete channel, while the lower sequence presents a magnified view of the region of interest. The initial image, designated as Frame 0, captures the structure that remains affixed to the filter surface. The 0–1 difference image accentuates the alterations between successive frames, with Frame 1 illustrating the structure's detachment. The isolated particle structure detached from the filter surface and was transported with the flow towards the end of the channel. Such relocations were, however, rare occurrences across all investigated carbon blacks.

The soot structures typically oxidized in place, forming fewer isolated structures than those observed by Sappok et al. Sappok et al. (2013) and Thieringer et al. Thieringer et al. (2023), with small isolated islands disappearing rapidly once exposed to the oxidizing gas flow. The total number of observed relocation events is quantified for all particle systems and is summarized in Fig. 10. Across all CB systems, the number of relocations ranged between 0–10 per experiment, independent of reactivity index. In contrast, PS-T817 exhibited substantially more frequent relocations, with 11 to 80 events depending on regeneration temperature Thieringer et al. (2023), Desens et al. (2025a). To put the results into context, it should be noted that there are minor differences in how the experiments were conducted in the two studies. In study of

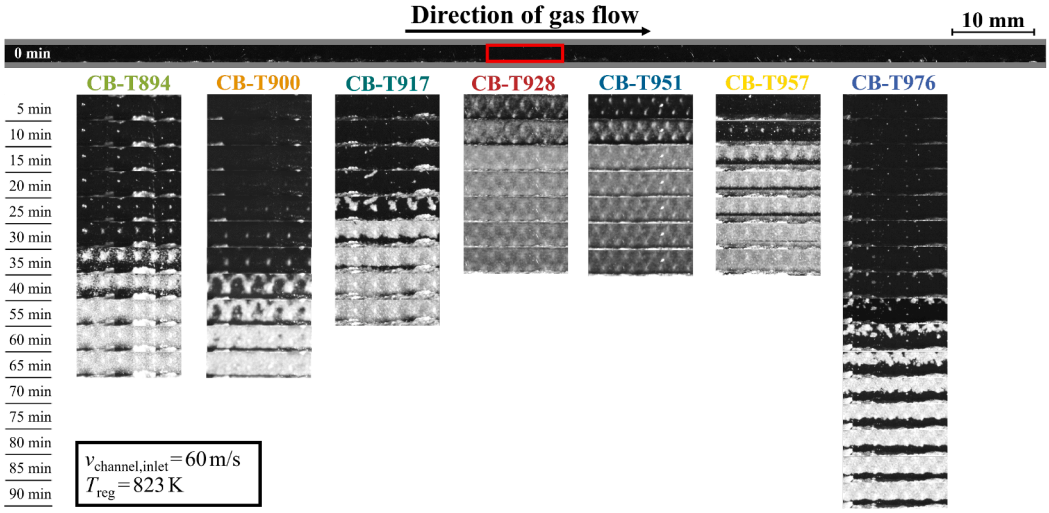

Fig. 6. Time-resolved image sequence of the regeneration process, showing the progression in the central channel region (marked in the 0 min frame of the complete channel) from 5 min to 90 min for the investigated carbon blacks (CB-T894 to CB-T976).

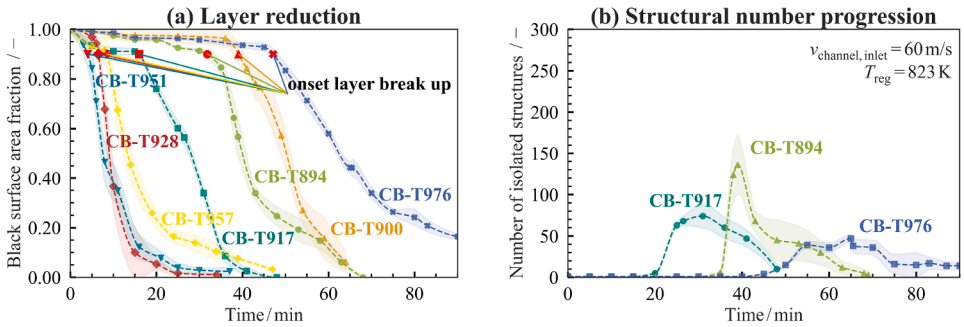

Fig. 7. a) Comparison of CB-T894 to CB-T976 black surface layer reduction over time with the marked onset of layer break-up b) Comparison of CB-T894, CB-T917 and CB-T976 structural number progression over time.

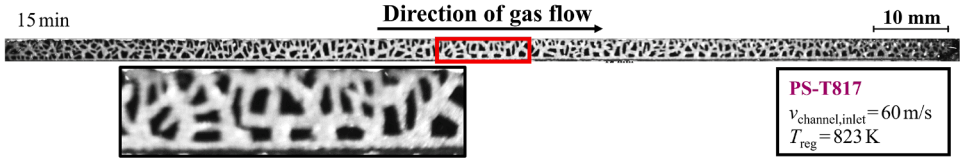

Fig. 8. Example frame from regeneration with the reactive soot system generated in fuel-rich propane combustion (PS-T817) Desens et al. (2025a), showing the clear formation of numerous individual particle structures.

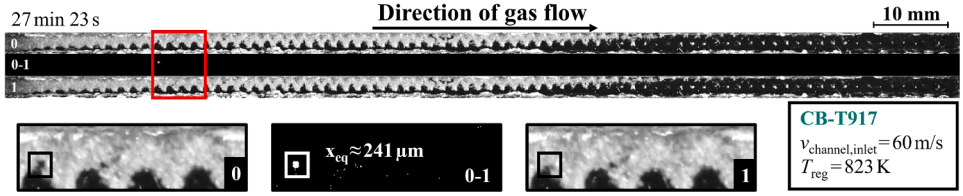

Fig. 9. The upper frames show the full channel during filter regeneration with CB-T917 at 27 min 23 s, while the lower sequence presents a magnified view of the marked region; Frame 0 captures the structure still attached to the filter surface. The 0–1 difference image highlights the change between consecutive frames, and subsequent Frame 1 shows the structure detached. Frame rate of the recording was 1000 fps.

Thieringer et al., regeneration began during the heating phase, meaning that a portion of soot oxidation occurred while the filter temperature was still increasing, and the indicated regeneration temperature describes the final temperature reached. In addition, the soot mass was 6 mg instead of the 10 mg examined here. In contrast, in the present study and in Desens et al. (2025a), the filter channel was preheated in an inert N_2 atmosphere, ensuring that the defined regeneration temperature was constant throughout the oxidation process.

The result for PS-T817 at 753 K from Thieringer et al. with a reduced reactivity index of 0.67 due to the lower regeneration temperature, showed a similar number of relocations to the CBs at a similar reactivity index. Whereas measurements at higher regeneration temperatures

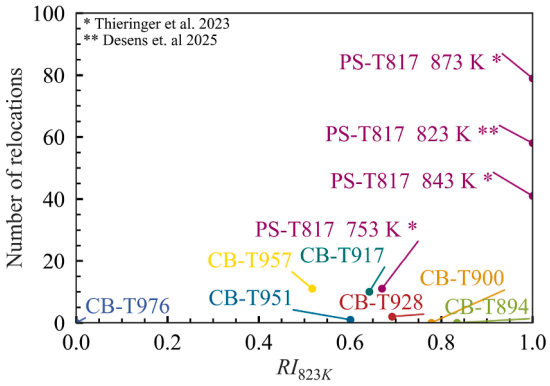

Fig. 10. Number of relocations of all carbon blacks CB-T894 to CB-T976 during filter regeneration (T_{reg} = 823 K, $v_{channel,inlet}$ = 60 m/s) over the reactivity index RI_{823K} and, for comparison, the results with PS-T817 (T_{reg} =753 K…873 K, $v_{channel,inlet}$ = 60 m/s) *Thieringer et al. (2023) **Desens et al. (2025a).

(823-873 K) show a pronounced increase in relocation frequency. This observation indicates that the combination of high reactivity and elevated regeneration temperature promotes detachment and downstream transport of soot fragments. When considering only the carbon blacks, no clear correlation between the number of relocations and the reactivity index (RI_{823K}) can be established, except that all of them show only few detachment events at these regeneration conditions.

3.2. Regeneration behavior of a specific carbonaceous particle system at different regeneration conditions

To further investigate the layer break-up one specific carbon black is selected: CB-T917, a carbon black with a primary particle size of 30 nm, representing a diesel-like primary particle size. This material had shown a few particle relocations during regeneration. It should be examined whether this carbon black changes its behavior under varying regeneration conditions (layer composition, layer height, regeneration temperature) and whether it can exhibit formation of isolated particle structures similar to PS-T817 and diesel soot with more detachment events. To examine the effect of compositional reactivity, a binary mixture of CB-T917 and CB-T976 (50 wt.% each) was prepared by shaking and stirring and was filled into the feed container with stirrer of the Topas disperser. The mixture was aerosolized and subsequently deposited in the model filter channel to form a layer with different reactive carbon blacks. Regeneration was also performed at 823 K and a gas velocity of 60 m/s. The resulting break-up and relocation behavior exhibited no significant deviation from that of the pure CB layers. Thieringer's investigations with propane derived soot showed that with increasing layer thickness, larger particle structures are formed during layer break-up, and the particle layer breaks up later Thieringer et al. (2023). Therefore, in a further series of tests, the layer thickness of CB-T917 was varied. Filters were prepared with initial soot-layer heights of approximately 250 µm, 210 µm, and 135 µm. The thinner layers showed a slightly accelerated oxidation response, an earlier onset of break-up and a faster regeneration time. However, the overall fragmentation and number of detached structures remained largely unchanged.

3.2.1. Variation of the temperature during regeneration

Research conducted by Thieringer et al. Thieringer et al. (2023) with propane derived soot has shown that increasing the regeneration temperature from 753 K to 873 K reduces the regeneration time by up to 55 % due to the faster oxidation of soot particles. Small particle structures form during layer reduction and the number of relocations increases with increasing regeneration temperature. Therefore, the temperature was varied to see whether CB-T917 exhibits similar behavior, especially at higher temperatures. The effect of regeneration temperature on oxidation dynamics and layer break-up behavior was investigated for CB-T917 at 723 K, 823 K, and 873 K under identical conditions (60 m/s, particle-free air). Based on the oxidation rate from the TPO they are classified in the reactivity index RI823K with increasing temperature as follows: 0.05 (723 K), 0.64 (823 K), and 0.97 (873 K).

Fig. 11 shows the time-resolved image sequences recorded in the central channel region comparing the progression of the particle layer. A clear temperature dependence of the regeneration rate is evident, the soot layer oxidizes as expected progressively faster with increasing temperature. The regeneration process is completed in 30 min at a regeneration temperature of 873 K, which is 40 % shorter than at 823 K. At 723 K, soot residues can still be seen in the rear section of the channel after 130 min. The oxidation front consistently progresses from the inlet toward the outlet, following the direction of gas flow. In Fig. 12 a) the quantitative analysis shows the normalized black surface area fraction decreasing markedly faster at higher temperatures. The onset points of layer break-up, indicated by red symbols, shift systematically to earlier times as temperature increases. At regeneration temperatures of 823 K and 873 K, the layer exhibits a greater tendency to form distinct structures in comparison to the regeneration at 723 K. The onset of layer break-up occurs earliest at 5 min (873 K), followed by 16 min (823 K) and 28 min (723 K). Fig. 12 b) depicts the corresponding progression of the number of isolated particle structures. The number of isolated structures is lowest at 723 K and increases at higher regeneration temperatures. The maxima at 823 K and 873 K are very similar, with a slightly higher peak count of about 75 structures at 823 K.

The number of observed relocation events for CB-T917 also increases slightly with temperature, from none at 723 K to 10 events at 823 K and 11 events at 873 K. This strengthens the hypothesis that structures must first be isolated in order to detach, as the particle-particle adhesive force is stronger than the particle-filter adhesive force Kamp et al. (2014). However, in the experiment at a regeneration temperature of 873 K, only a few rearrangements could be observed despite a comparable reactivity index of 0.97 to 1.00 for PS-T817 at 823 K. These results show that even at comparable soot reactivity and temperature, layer break-up with relocation cannot be explained by oxidation of the carbonaceous particles alone, but requires additional triggers associated with the presence of SOF. Experimental fragmentation measurements by Rothenbacher et al. Rothenbacher et al. (2008) quantified the cohesive strength of diesel-soot agglomerates and the effect of condensed adsorbates. They reported 50 % fragmentation energies of 5.2×10^{-17} J for thermodenuded ("dried") diesel soot and 1.2×10^{-1} J for untreated soot, i.e. the presence of adsorbates almost doubles the mean bond strength. In contrast, the calculated van der Waals bond energy for a typical soot agglomerate with 90 primary particles was only 5.5×10^{-19} J, so that the measured fragmentation energies exceed the pure van der Waals force by factors of roughly 95 (dried) and 220 (with adsorbates). During regeneration, desorption and early oxidation of SOF may trigger local oxidation and modify the nanomechanical stability of the soot layer, promoting layer break-up, and facilitate the detachment of smaller particle structures.

3.2.2. Potential influence of more reactive by-Products of the combustion process

As outlined in the introduction, engine-derived soot and PS-T817 typically carry a condensed organic fraction (SOF/VOF) containing semi-volatile HCs, PAHs, and traces of water, whereas the selected carbon blacks are essentially ash-free and largely depleted in condensed organics. To assess the potential influence of such condensed by-products, additional regeneration tests were performed with CB-T917 under modified conditions. Experiments with injected or condensed water on the soot layer showed no measurable change in regeneration behavior, indicating that the added water most likely evaporated during the heating phase without significantly affecting layer break-up or relocations. Another series of experiments was conducted to simulate the presence

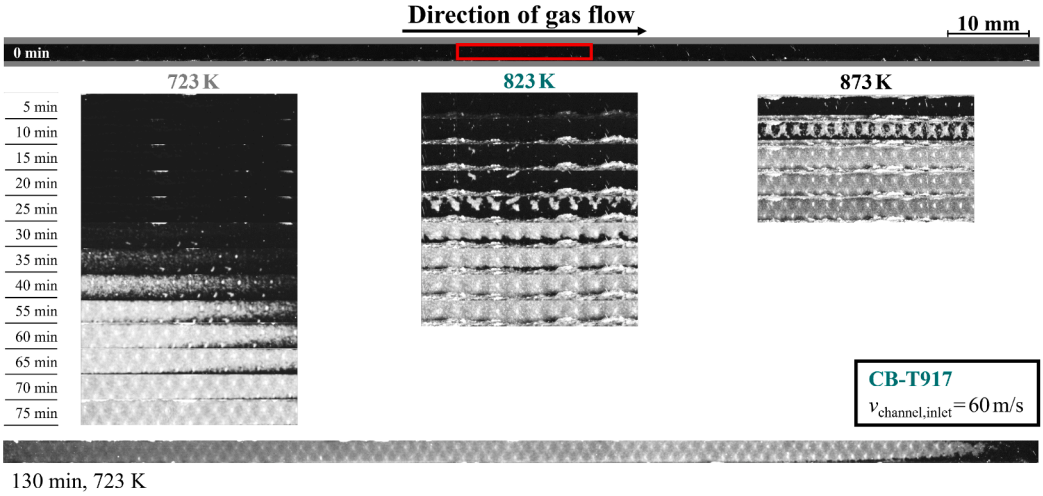

Fig. 11. Time-resolved image sequence of the regeneration process, showing the progression in the central channel region (marked in the frame at 0 min) from 5 min to 75 min for CB-T917 at 723 K, 823 K and 873 K, respectively.

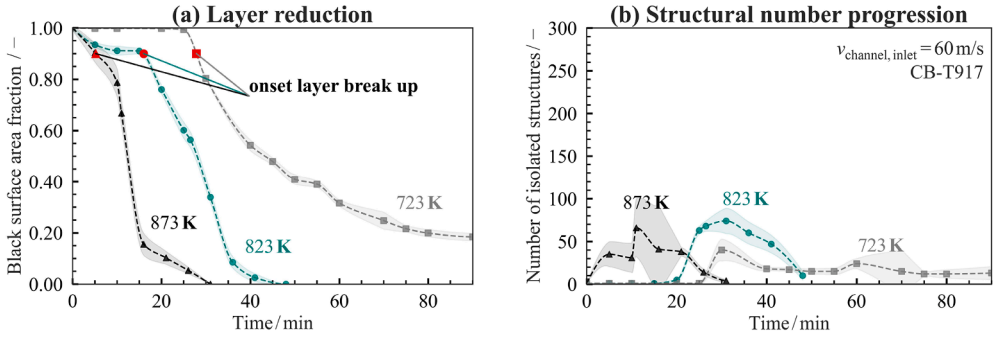

Fig. 12. Comparison of CB-T917 at 723 K, 823 K and 873 K a) total layer reduction over time with the marked onset of layer break-up b) structural number progression over time.

Fig. 13. Observation of the evaporation of hydrocarbons during heating at ~500 K in a N_2 atmosphere.

of condensed hydrocarbons typically found in engine-generated soot (e.g., naphthalene, phenanthrene, pyrene, benzo[a]pyrene) Geldenhuys et al. (2022), Hu et al. (2013). For safety and reproducibility, a model hydrocarbon mixture (Hydrocarbon mixture C_{10}-C_{13}, > 30 % aliphatic hydrocarbons, 15–30 % aromatic hydrocarbons, containing white spirit 180/210) was used with a boiling range of 453–483 K. This reliably wets carbon black and forms a hydrophobic organic coating, while remaining free of ash or impurities. Although this system does not fully replicate the chemical complexity of diesel soot, it provides a controlled means of assessing whether highly reactive organic species affect oxidation or detachment behavior. For sample preparation, filters were loaded with dry CB T917 at ambient temperature as described previously. Subsequently, fine droplets of the hydrocarbon mixture (~30 wt.%) were sprayed with a nozzle onto the soot layer. The CB layer containing the hydrocarbon mixture was subjected to a purge of compressed air at a velocity of 5 m/s for a duration of 1 h at ambient temperature. This was followed by a 24 h equilibration period, the purpose of which was to achieve a homogeneous distribution of the mixture within the CB layer. Regeneration was then carried out again under identical boundary conditions (823 K, 60 m/s, particle-free air).

During the heating phase in an N_2 atmosphere at approximately 500 K, parts of the hydrocarbon fraction undergo visible evaporation, as illustrated in Fig. 13. After a few minutes, the surface of the channel reverts to its original black state, becoming visibly indistinguishable from untreated CB Layers. A similar effect was reported by Thieringer et al. Thieringer et al. (2023) for propane derived soot, where volatile components desorbed during the heating phase. The regeneration behavior of CB-T917 changes profoundly, as illustrated in Fig. 14. Initially, the filter surface is covered with the carbon black and appears completely black. Between 6 min and 18 min, the layer breaks up into numerous discrete particle structures. To capture this transient phase, frames are displayed at 2 min intervals and with enlarged views of the central channel region every 4 min.

The images clearly show the formation of multiple small isolated particle structures that gradually shrink or vanish from the field of view, many of which detach and migrate downstream, while others oxidize locally. After 20 min, less than 10 % of the soot remains, localized mainly in the rear third of the channel, and after 40 min, the filter is nearly clean. The high-speed recordings are also quantitatively evaluated using image analysis and compared with the filter regeneration of the same carbon black without the additional hydrocarbons (see Fig. 15). The results mirror these observations: For the HC treated sample the layer break-up initiates earlier (4.5 min vs. 16 min), the regeneration completes more rapidly, and the number of isolated distinct particle structures rises sharply (~75 → ~1100). This indicates that the presence of the more reactive hydrocarbons in this experiment accelerate local oxidation by modifying surface reactivity. The high-speed recordings at 1000 fps of the model filter channel regeneration with CB-T917

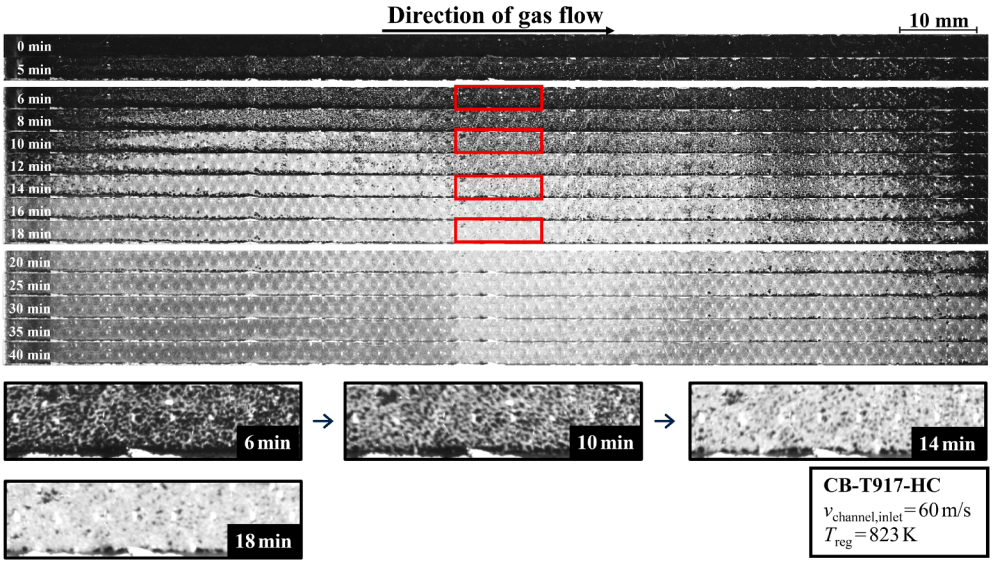

Fig. 14. Time-resolved image sequence of the regeneration process of CB-T917-HC, illustrating the progression from the initiation of regeneration 0 min to 40 min over the entire channel length. The marked regions are shown magnified below, illustrating the oxidation of structural sizes between 6 min and 18 min.

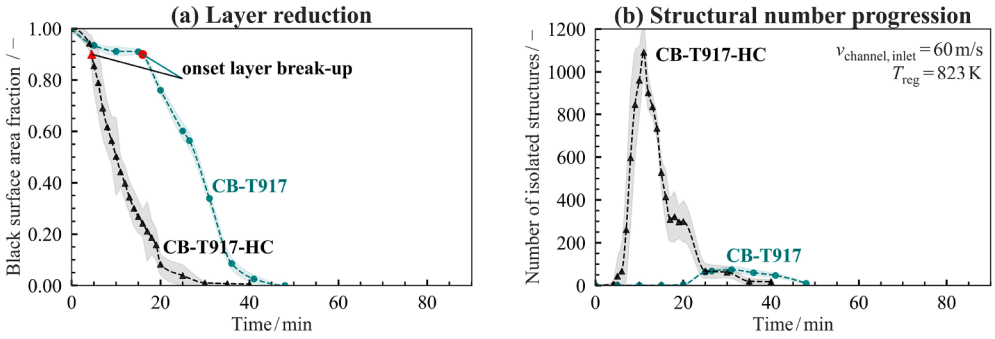

Fig. 15. Comparison of CB-T917 and CB-T917-HC with the hydrocarbon mixture a) total layer reduction over time with the marked onset of layer break-up b) structural number progression over time.

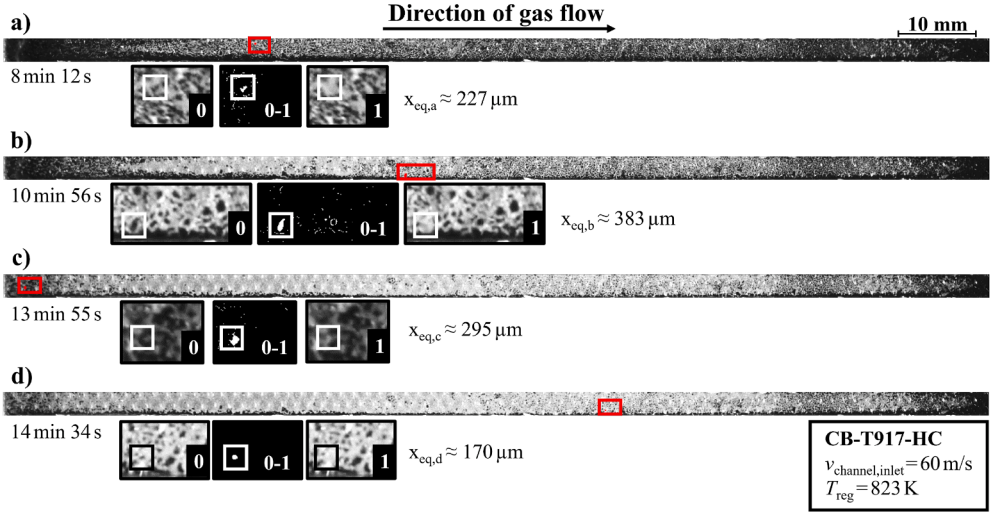

Fig. 16. a-d) Exemplary particle structure detachment events observed during filter regeneration with CB T917-HC coated with the hydrocarbon mixture. The upper frames show the full channel at the respective time of detachment, while the lower sequences present magnified views of the marked regions. In each case, Frame 0 (left) captures the structure still attached to the filter surface, the 0–1 difference image (center) highlights the change between consecutive frames, and Frame 1 (right) shows the detached structure. Frame rate of the recording was 1000 fps.

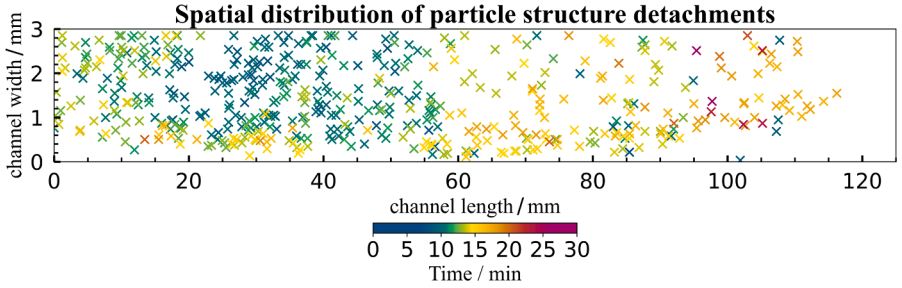

Fig. 17. Spatial distribution of particle detachment events along the channel length for CB-T917 coated with the hydrocarbon mixture. Color coding indicating the detachment time.

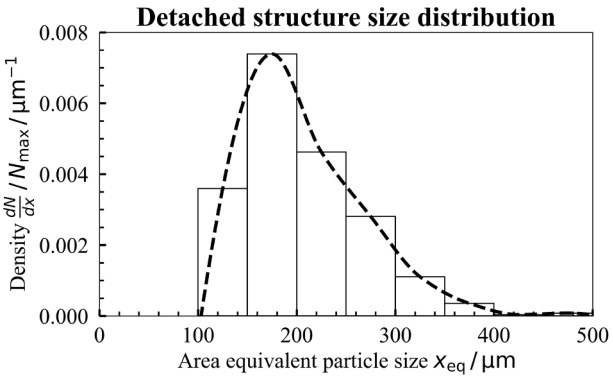

Fig. 18. Number-based particle size distribution of the detached particle structures during the regeneration of the model filter channel for CB-T917 coated with the HC mixture.

HC reveal numerous particle detachment events, as demonstrated by four examples shown in Fig. 16 at different times and positions along the channel. Each frame shows the full channel view before the respective detachment event and a magnified region of interest, recorded at 1000 fps. In each magnified example, Frame 0 captures the particle structure still attached to the filter surface, the 0–1 difference image visualizes the change between consecutive frames, and Frame 1 shows the location of the missing structure after detachment. In Fig. 16 a), a particle structure with an area equivalent diameter of 227 µm detaches after 8 min 12 s in the front third of the channel (30.5 mm). Fig. 16 b) captures a larger structure detaching after 10 min 56 s near the channel center, while c) shows one separating from the surface at 13 min 55 s near the inlet. Finally, d) depicts the detachment of a smaller particle structure ($x_{eq,d} \approx 170$ µm) in the rear half of the channel after 14 min 34 s. In total, ≥ 507 of such events were detected, involving structures with $x_{eq} \geq 100$ µm, while even smaller particle structures might escape detection due to the set threshold and the limited resolution. As mapped in Fig. 17, detachment events are widely distributed along the channel length. Detachment events are concentrated within a 20 min period and occur most frequently in the front half of the channel. This is where the gas velocity is highest, which increases the probability of the detachment of particle structures from the filters surface. Towards the end of the channel, the number of detachments decreases, and these usually occur at later stages of regeneration. However, some structures remain intact for longer at the channel inlet for up to 14 min. This could be due to the HC distribution, as the flow might have carried them more towards the center of the channel causing less reactive components to break up the layer. Fig. 18 shows the number-based particle size distribution of detached structures detected during the regeneration with CB T917 HC. The distribution spans an area equivalent diameter range from 100 µm to 500 µm, with the majority of detected particle structures between 150 µm and 200 µm. Comparable characteristic size ranges for detached soot fragments were also reported by Thieringer et al. Thieringer et al. (2023, 2022) during regeneration experiments with propane derived soot and by Sappok et al. Sappok et al. (2013) for diesel soot particle layers. These findings do not conclusively verify that the presence of highly reactive SOF is essential for layer break-up and relocation phenomena. In this scenario, the accelerated oxidation and increased number of detachment events are not, or only partially, caused by sustained heat release from organic oxidation, but are more plausibly linked to improved gas accessibility and mechanical destabilization of the soot layer induced by liquid droplets and evaporation-driven restructuring. Trace amounts of oxygen in the nominally nitrogen-purged system cannot be fully excluded and may contribute to minor oxidation of the HC mixture during the initial heating phase.

4. Conclusion and outlook

The combination of high-speed imaging with image analysis enabled a detailed characterization of layer break-up and particle relocation dynamics. Comparative analysis of seven carbon blacks revealed pronounced differences in oxidation behavior, layer break-up, and detachment frequency than PS-T817 and diesel soot. More reactive carbon blacks exhibited faster oxidation and earlier onset of layer break-up, while the least reactive Carbon Black CB-T976 showed gradual burnoff. All carbon blacks showed a reduction in surface layer coverage with little break-up and formation of isolated structures as well as minimal relocation activity. Variations in temperature confirmed that thermal activation accelerates oxidation kinetics but does not fundamentally alter the fragmentation pattern for the carbon black CB-T917. In contrast, the addition of a more reactive hydrocarbon mixture (C_{10}-C_{13}, > 30 % aliphatic hydrocarbons, 15–30 % aromatic hydrocarbons, containing white spirit 180/210) significantly led to enhanced layer break-up, frequent detachment events with more than 500 particle structures relocating, and faster overall regeneration.

The model filter channel experiments provide fundamental research with well-defined particle systems linking soot reactivity and layer composition to layer break-up and relocation frequency. The results indicate that the reactivity of carbonaceous particles alone mainly governs the rate of soot removal, whereas pronounced fragmentation and relocation are more likely driven by additional more reactive or condensed species affecting layer mechanics and gas accessibility. Such relocation activity is relevant for aftertreatment design because repeated transport and redeposition can shift deposits toward plug-end/channel-filling patterns, which affect pressure drop and filtration behavior. Therefore, regeneration strategies should consider fuel- and operation-dependent variations in soot composition, as these may contribute to more relocations of particle structures. Since soot nanostructure and reactivity are known to vary with engine operating conditions Koch et al. (2022), Hagen et al. (2023), the results can be transferred to real exhaust by relating operating-point-induced changes in soot.

Future work will focus on systematically assessing the influence of condensed organic fractions on soot layer break-up and relocation phenomena. This might include controlled desorption experiments using diesel

or propane derived soot to quantify the effect of organic components on adhesion and break-up behavior. In addition, the oxidation atmosphere will be varied between O_2- and NO_2-rich conditions over a range of regeneration temperatures to evaluate the effects of the oxidizing agents on the regeneration phenomena. The NO_2 rich atmosphere enhances the soot oxidation at lower temperatures Müller et al. (2012). The working hypothesis is that discontinuous NO_2 regeneration at lower temperatures (523-823 K) can trigger layer break-up and relocation behavior comparable to that observed during discontinuous O_2 regeneration at higher temperatures (723-873 K). More generally, the objective is to clarify whether, and under which conditions, the interplay between oxidation gas (O_2 vs. NO_2), soot reactivity and dispersity, and operating parameters governs the transition between layer-type deposition and channel plugging after repeated regenerations.

Declaration of generative AI use

During the preparation of this work the authors used "ChatGPT-5" and "DeepL Write" in order to refine the language with grammar and punctuation corrections. After using these tools, the authors reviewed and edited the content as needed and take full responsibility for the content of the publication.

CRediT authorship contribution statement

Ole Desens: Writing – original draft, Visualization, Validation, Software, Methodology, Investigation, Formal analysis, Data curation; **Özge Yavuz:** Writing – review & editing, Investigation, Formal analysis; **Fabian P. Hagen:** Writing – review & editing, Investigation, Conceptualization; **Jörg Meyer:** Writing – review & editing, Conceptualization; **Achim Dittler:** Writing – review & editing, Supervision, Resources, Funding acquisition, Conceptualization.

Data availability

Data will be made available on request.

Declaration of competing interest

The authors declare no Conflict of interests or personal relationships that could have appeared to influence the work reported in this paper.

Acknowledgment

The authors are very grateful to the Deutsche Forschungsgemeinschaft (DFG, German Research Foundation) for financial support within the project 438308378.

References

Alhikami, A.F., Wang, W., Nugroho, R. A.A., Hsieh, H., 2022. Experimental studies of soot formation for petro- and renewable diesels. Int. J. Energy Res. 46 (13), 19109–19122. https://doi.org/10.1002/er.8223

Bensaid, S., Marchisio, D.L., Fino, D., 2010. Numerical simulation of soot filtration and combustion within diesel particulate filters. Chem. Eng. Sci. 65 (1), 357–363. https://doi.org/10.1016/j.ces.2009.06.051

Boehman, A.L., Song, J., Alam, M., 2005. Impact of biodiesel blending on diesel soot and the regeneration of particulate filters. Energy Fuels 19 (5), 1857–1864. https://doi.org/10.1021/ef0500585

Böhmeke, C., Wagner, U., Koch, T., 2024. Influence of the air-fuel-ratio and fuel on the reactivity of diesel soot. Automot. Engine Technol. 9 (1), 07. https://doi.org/10.1007/s41104-024-00145-3

Chen, C., Fan, X., Shaltout, T., Qiu, C., Ma, Y., Goldman, A., Khalizov, A.F., 2016. An unexpected restructuring of combustion soot aggregates by subnanometer coatings of polycyclic aromatic hydrocarbons. Geophys. Res. Lett. 43 (20). https://doi.org/10.1002/2016GL070877

Chen, H., Ji, Z., Wang, X., Pan, M., Yi, C., Zhang, P., 2024. Investigation of the nanostructure and reactivity of soot particulates from diesel/methanol dual-fuel combustion with and without egr. Sustain. Energy Fuels 8 (5), 1012–1023. https://doi.org/10.1039/D3SE01701J

Choi, S., Oh, K.-C., Lee, C.-B., 2014. The effects of filter porosity and flow conditions on soot deposition/oxidation and pressure drop in particulate filters. Energy 77, 327–337. https://doi.org/10.1016/j.energy.2014.08.049

Clague, A., Donnet, J., Wang, T., Peng, J., 1999. A comparison of diesel engine soot with carbon black. Carbon N Y 37 (10), 1553–1565. https://doi.org/10.1016/S0008-6223(99)00035-4

Corbin, J.C., Modini, R.L., Gysel-Beer, M., 2023. Mechanisms of soot-aggregate restructuring and compaction. Aerosol Sci. Technol. 57 (2), 89–111. https://doi.org/10.1080/02786826.2022.2137385

Cui, Y., Cai, Y., Fan, R., Shi, Y., Gu, L., Pu, X., Tian, J., 2018. Effects of residual ash on dpf capture and regeneration. Int. J. Automot. Technol. 19 (5), 759–769. https://doi.org/10.1007/s12239-018-0073-5

Desens, O., Hagen, F.P., Meyer, J., Dittler, A., 2025a. In Situ Observation of Different Soot Layers in a Model Filter Channel during Its Regeneration. https://doi.org/10.4271/2025-01-0312

Desens, O., Meyer, J., Dittler, A., 2025b. Application of python image analysis tools for particle structure detachment detection in high-speed videos during model filter regeneration. MethodsX 15, 103598. https://doi.org/10.1016/j.mex.2025.103598

Dittler, A., 2017. The application of diesel particle filters-from past to present and beyond. Top. Catal. 60 (3–5), 342–347. https://doi.org/10.1007/s11244-016-0621-z

Ess, M.N., Bladt, H., Mühlbauer, W., Seher, S.I., Zöllner, C., Lorenz, S., Brüggemann, D., Nieken, U., Ivleva, N.P., Niessner, R., 2016. Reactivity and structure of soot generated at varying biofuel content and engine operating parameters. Combust. Flame 163, 157–169. https://doi.org/10.1016/j.combustflame.2015.09.016

European Commission, Regulation (EC) No 715/2007 of the European Parliament and of the Council of 20 June 2007 on type approval of motor vehicles with respect to emissions from light passenger and commercial vehicles. European Commission. 2020.

European Commission. Directorate General for Environment, Air quality monitoring for air quality policy: technical support document on the use of reference and non reference methods, and on the quality assurance process to meet relevant data quality objectives for regulated air pollutants : final version. Publications Office, LU. 2025.

Frank, R.W., Hardenberg, H.O., 1985. Reduction of particulate emission from the break-in facilities of a heavy-duty engine plant by means of ceramic monolith traps. SAE Tech. Paper 850268. https://doi.org/10.4271/850268

Fu, Z., Fan, C., Liu, Y., Guan, Z., Wei, M., Xu, B., Shang, T., Shang, W., 2026. Insights into the oxidation regime of diesel soot during realistic dpf regeneration. Fuel 403, 136086. https://doi.org/10.1016/j.fuel.2025.136086

Gaiser, G., Mucha, P., 2004. Prediction of Pressure Drop in Diesel Particulate Filters Considering Ash Deposit and Partial Regenerations, SAE Technical Paper. https://doi.org/10.4271/2004-01-0158

Geldenhuys, G., Wattrus, M., Forbes, P., 2022. Gas and particle phase polycyclic aromatic hydrocarbon emission factors from a diesel vehicle engine: effect of operating modes in a developing country context. Atmos. Environ.: X 13, 100158. https://doi.org/10.1016/j.aeaoa.2022.100158

Ghiassi, H., Toth, P., Jaramillo, I.C., Lighty, J.S., 2016. Soot oxidation-induced fragmentation: part 1: the relationship between soot nanostructure and oxidation-induced fragmentation. Combust. Flame 163, 179–187. https://doi.org/10.1016/j.combustflame.2015.09.023

Gogoi, B., Raj, A., Alrefaai, M.M., Stephen, S., Anjana, T., Pillai, V., Bojanampati, S., 2015. Effects of 2,5-dimethylfuran addition to diesel on soot nanostructures and reactivity. Fuel 159, 766–775. https://doi.org/10.1016/j.fuel.2015.07.038

Hafen, N., Marquardt, J.E., Dittler, A., Krause, M.J., 2023. Simulation of particulate matter structure detachment from surfaces of wall-flow filters for elevated velocities applying lattice boltzmann methods. Fluids 8 (3), 99. https://doi.org/10.3390/fluids8030099

Hagen, F., Hardock, F., Koch, S., Sebbar, N., Bockhorn, H., Loukou, A., Kubach, H., Suntz, R., Trimis, D., Koch, T., 2021a. Why soot is not alike soot: a molecular/nanostructural approach to low temperature soot oxidation. Flow, Turbul. Combust. 106 (2), 295–329. https://doi.org/10.1007/s10494-020-00205-2

Hagen, F.P., Kretzler, D., Häber, T., Bockhorn, H., Suntz, R., Trimis, D., 2021b. Carbon nanostructure and reactivity of soot particles from non-intrusive methods based on UV–vis spectroscopy and time-resolved laser-induced incandescence. Carbon N Y 182, 634–654. https://doi.org/10.1016/j.carbon.2021.06.006

Hagen, F.P., Kretzler, D., Koch, S., Bockhorn, H., Suntz, R., Trimis, D., Kubach, H., Velji, A., Koch, T., 2023. On-line monitoring of carbon nanostructure and soot reactivity in engine exhaust by dual-pulse laser-induced incandescence. Combust. Flame 254, 112850. https://doi.org/10.1016/j.combustflame.2023.112850

Hu, S., Herner, J.D., Robertson, W., Kobayashi, R., Chang, M.-C.O., Huang, S.-M., Zielinska, B., Kado, N., Collins, J.F., Rieger, P., Huai, T., Ayala, A., 2013. Emissions of polycyclic aromatic hydrocarbons (pahs) and nitro-pahs from heavy-duty diesel vehicles with dpf and scr. J. Air Waste Manag. Assoc. 63 (8), 984–996. https://doi.org/10.1080/10962247.2013.795202

Huang, J., Gao, J., Gao, J., Huang, Y., Wang, X., Wang, S., Qi, M., Tian, G., 2024. Insight into the mechanism of solution organic fractions on soot oxidation activity enhancement. J. Hazard. Mater. 479, 135606. https://doi.org/10.1016/j.jhazmat.2024.135606

Ishizawa, T., Yamane, H., Satoh, H., Sekiguchi, K., Arai, M., Yoshimoto, N., Inoue, T., 2009. Investigation into ash loading and its relationship to dpf regeneration method,. SAE Int. J. Commer. Veh. 02 (2), 164–175. https://doi.org/10.4271/2009-01-2882

Kamp, C.J., Sappok, A., Wang, Y., Bryk, W., Rubin, A., Wong, V., 2014. Direct measurements of soot/ash affinity in the diesel particulate filter by atomic force microscopy and implications for ash accumulation and dpf degradation,. SAE Int. J. Fuels Lubr. 7 (1), 307–316. https://doi.org/10.4271/2014-01-1486

Kelesidis, G.A., Pratsinis, S.E., 2019. Estimating the internal and surface oxidation of soot agglomerates. Combust. Flame 209, 493–499. https://doi.org/10.1016/j.combustflame.2019.08.001

Knauer, M., Schuster, M.E., Su, D., Schlögl, R., Niessner, R., Ivleva, N.P., 2009. Soot structure and reactivity analysis by raman microspectroscopy, temperature-programmed oxidation, and high-resolution transmission electron microscopy. J. Phys. Chem. A 113 (50). https://doi.org/10.1021/jp905639d

Koch, S., Hagen, F.P., Büttner, L., Hartmann, J., Velji, A., Kubach, H., Koch, T., Bockhorn, H., Trimis, D., Suntz, R., 2022. Influence of global operating parameters on the reactivity of soot particles from direct injection gasoline engines. Emission Control Sci. Technol. 8 (1–2), 9–35. https://doi.org/10.1007/s40825-022-00211-y

Konstandopoulos, A.G., Johnson, J.H., 1989. Wall-Flow Diesel Particulate Filters-Their Pressure Drop and Collection Efficiency, SAE Technical Paper 890405. https://doi.org/10.4271/890405

Lapuerta, M., Oliva, F., Agudelo, J.R., Boehman, A.L., 2012. Effect of fuel on the soot nanostructure and consequences on loading and regeneration of diesel particulate filters. Combust. Flame 159 (2), 844–853. https://doi.org/10.1016/j.combustflame.2011.09.003

Levenberg, K., 1944. A method for the solution of certain non-linear problems in least squares. Q. top. Q. Appl. Math. 2 (2), 164–168. https://doi.org/10.1090/qam/10666

Liati, A., Eggenschwiler, P.D., Schreiber, D., Zelenay, V., AmmannM., 2013. Variations in diesel soot reactivity along the exhaust after-treatment system, based on the morphology and nanostructure of primary soot particles. Combust. Flame 160 (3), 671–681. https://doi.org/10.1016/j.combustflame.2012.10.024

Lindner, S., Massner, A., Gärtner, U., Koch, T., 2015. Impact of engine combustion on the reactivity of diesel soot from commercial vehicle engines. Int. J. Engine Res. 16 (1), 104–111. https://doi.org/10.1177/1468087414563360

Liu, Y., Song, C., Lv, G., Wang, X., Li, N., 2017. Virgin and extracted soots in premixed methane flames: a comparison of surface functional groups, graphitization degree, and oxidation reactivity. Energy Fuels 31 (6), 6413–6421. https://doi.org/10.1021/acs.energyfuels.6b03011

MaricqM.M., 2007. Chemical characterization of particulate emissions from diesel engines: a review. J. Aerosol Sci. 38 (11), 1079–1118. https://doi.org/10.1016/j.jaerosci.2007.08.001

Mahrt, F., Marcolli, C., David, R.O., Grönquist, P., Meier, E. J.B., Lohmann, U., Kanji, Z.A., 2018. Ice nucleation abilities of soot particles determined with the Horizontal Ice Nucleation Chamber. https://doi.org/10.5194/acp-2018-557

Marquardt, D.W., 1963. An Algorithm for Least-Squares Estimation of Nonlinear Parameters. Vol. 11. Society for Industrial and Applied Mathematics.

Messerer, A., Niessner, R., Pöschl, U., 2006. Comprehensive kinetic characterization of the oxidation and gasification of model and real diesel soot by nitrogen oxides and oxygen under engine exhaust conditions: measurement, langmuir-hinshelwood, and arrhenius parameters. Carbon N Y 44 (2), 307–324. https://doi.org/10.1016/j.carbon.2005.07.017

Müller, J.-O., Frank, B., Jentoft, R.E., Schlögl, R., Su, D.S., 2012. The oxidation of soot particulate in the presence of no2. Catal. Today 191 (1), 106–111. https://doi.org/10.1016/j.cattod.2012.03.010

Parliament, E., . Regulation (EU) 2024/1257 of the European Parliament and of the council on type-approval of motor vehicles and engines and of systems, components and separate technical units intended for such vehicles, with respect to their emissions and battery durability. 2024

Rothenbacher, S., Messerer, A., Kasper, G., 2008. Fragmentation and bond strength of airborne diesel soot agglomerates. Part Fibre Toxicol. 5 (1), 9. https://doi.org/10.1186/1743-8977-5-9

Sappok, A., Govani, I., Kamp, C., Wang, Y., Wong, V., 2013. In-Situ optical analysis of ash formation and transport in diesel particulate filters during active and passive DPF regeneration processes 6, 336–349. https://doi.org/10.4271/2013-01-0519

Sappok, A., Wang, Y., Wang, R.-Q., Kamp, C., Wong, V., 2014. Theoretical and experimental analysis of ash accumulation and mobility in ceramic exhaust particulate filters and potential for improved ash management. SAE Int. J. Fuels Lubr. 07 (2), 511–524. https://doi.org/10.4271/2014-01-1517

Schmid, J., Grob, B., Niessner, R., Ivleva, N.P., 2011. Multiwavelength raman microspectroscopy for rapid prediction of soot oxidation reactivity. Anal. Chem. 83 (4), 1173–1179. https://doi.org/10.1021/ac102939w

Schnitzler, E.G., Gac, J.M., Jäger, W., 2017. Coating surface tension dependence of soot aggregate restructuring. J. Aerosol. Sci. 106, 43–55. https://doi.org/10.1016/j.jaerosci.2017.01.005

Shao, C., Wang, Q., Zhang, W., Bennett, A., Li, Y., Guo, J., Im, H.G., Roberts, W.L., Violi, A., Sarathy, S.M., 2023. Elucidating the polycyclic aromatic hydrocarbons involved in soot inception. Commun. Chem. 6 (1), 223. https://doi.org/10.1038/s42004-023-01017-x

Sharma, H.N., Pahalagedara, L., Joshi, A., Suib, S.L., Mhadeshwar, A.B., 2012. Experimental study of carbon black and diesel engine soot oxidation kinetics using thermogravimetric analysis. Energy Fuels 26 (9), 5613–5625. https://doi.org/10.1021/ef3009025

Song, J., Alam, M., Boehman, A., Kim, U., 2006. Examination of the oxidation behavior of biodiesel soot. Combust. Flame 146 (4), 589–604. https://doi.org/10.1016/j.combustflame.2006.06.010

Soriano, J.A., Agudelo, J.R., López, A.F., Armas, O., 2017. Oxidation reactivity and nanostructural characterization of the soot coming from farnesane - a novel diesel fuel derived from sugar cane. Carbon N Y 125, 516–529. https://doi.org/10.1016/j.carbon.2017.09.090

Tandon, P., Heibel, A., Whitmore, J., Kekre, N., Chithapragada, K., 2010. Measurement and prediction of filtration efficiency evolution of soot loaded diesel particulate filters. Chem. Eng. Sci. 65 (16), 4751–4760. https://doi.org/10.1016/j.ces.2010.05.020

Thieringer, J. R.D., Hafen, N., Meyer, J., Krause, M.J., Dittler, A., 2022. Investigation of the rearrangement of reactive-inert particulate structures in a single channel of a wall-flow filter. Separations 9 (8), 195. https://doi.org/10.3390/separations9080195

Thieringer, J. R.D., Werling, H., Meyer, J., Dittler, A., 2023. In Situ tracking of Break-up, resuspension, and transport of reactive particle structures in a single Wall-Flow filter channel 9, 149–165. https://doi.org/10.1007/s40825-023-00228-x

Wal, R. L.V., Tomasek, A.J., 2003. Soot oxidation. Combust. Flame 134 (1–2), 1–9. https://doi.org/10.1016/S0010-2180(03)00084-1

Zainol, M.M., Abidin, A., Mustaffa, N., Rahman, S. N. F. S.A., Azli, A. A.M., Mustapa, A.N., Mamat, M.H., Syed-Hassan, S. S.A., Ali, N.H., Ahmad, M.H., Hamdan, K., 2025. A review on carbon black production, properties, and its applications toward energy storage. Energy 340, 139123. https://doi.org/10.1016/j.energy.2025.139123

Zhang, X., Song, C., Lyu, G., Li, Y., Qiao, Y., Li, Z., 2022. Physicochemical analysis of the exhaust soot from a gasoline direct injection (gdi) engine and the carbon black. Fuel 322, 124262. https://doi.org/10.1016/j.fuel.2022.124262

Zhou, R., Wang, S., Zhao, W., Li, J., Wu, S., Yang, W., 2025. A comparative study on the soot formation characteristics of dual-fuel engines fueled with n-butanol. Energy Sources Part A 47 (2). https://doi.org/10.1080/15567036.2025.2546525. https://doi.org/10.1080/15567036.2025.2546525